Supplementary Information (SI) for Journal of Materials Chemistry C.
This journal is © The Royal Society of Chemistry 2026

Supporting Information

Neutron Reflectometry for In-Depth Porosity and Figure-of-Merits Correction of Organic Electrochemical Transistors

Yi-Hsuan Tung,[a] *Tzu-Yen Huang,*[b] *Guo-Hao Jiang,*[a] *Shang-Wen Su,*[a] *Yan-Cheng Lin*[a,c,*]

[a] Department of Chemical Engineering, National Cheng Kung University, Tainan City 70101, Taiwan.

[b] Neutron Group, National Synchrotron Radiation Research Center, Hsinchu 30092, Taiwan.

[c] Advanced Research Center for Green Materials Science and Technology, National Taiwan University, Taipei 10617, Taiwan.

Corresponding Author's E-mail: ycl@gs.ncku.edu.tw (Y.-C. L.)

Experimental Section

Materials: Regioregular poly(3-hexylthiophene-2,5-diyl) (P3HT, UR-P3H001, purity > 99%, MW = 50,000–72,000) was purchased from Uni-Region Bio-Tech. Chlorobenzene (≥99.8%) was sourced from Sigma-Aldrich. Chloroform (≥99.8%) was obtained from Honeywell. Acetonitrile (ACN, ≥99.6%), potassium hexafluorophosphate (KPF_6, ≥99.0%), Tetra-*n*-butylammonium hexafluorophosphate ($TBAPF_6$, 98%), and 18-crown-6 (18-O-6, 99%) were obtained from Thermo Scientific.

Optical and Morphological Characterizations: The UV–Vis–NIR absorption spectra of the polymer films were measured using a JASCO V770 spectrophotometer. Electrochemical analyses of doped and dedoped films were conducted using a CHI 6273E electrochemical analyzer, employing a three-electrode configuration in 0.1 M KPF_6 electrolyte. A polymer-coated silicon wafer served as the working electrode, with platinum foil and an Ag/AgCl electrode acting as the counter and reference electrodes, respectively. Atomic force microscopy (AFM) imaging was performed using a Bruker Multifunctional Scanning Probe Microscope in tapping mode. Height images were acquired over multiple representative regions of each film under consistent scan parameters to ensure statistical reliability. The raw topography maps were first subjected to plane and line flattening to remove background tilt. Outlier pixels were suppressed using histogram-based intensity clipping to minimize spike artifacts. Surface coverage was then quantified using an adaptive global thresholding approach (Otsu-type) applied to the processed height maps. The same segmentation criteria were maintained across all images within each sample. Small isolated features below a predefined area threshold were removed to reduce noise-driven misclassification. The coverage ratio was calculated as the fractional segmented area relative to the total scan area, and the reported values represent the average across multiple independent scans. Grazing-incidence wide-angle X-ray scattering (GIWAXS) measurements were carried out at the BL13A1 beamline at the National Synchrotron Radiation Research Center (NSRRC), Taiwan, using an incident angle of 0.12° and an X-ray wavelength of 1.027 Å. Neutron reflectometry (NR) measurements were conducted at the Australian Nuclear

Science and Technology Organisation (ANSTO), using the SPATZ time-of-flight reflectometer. This facility enabled high-resolution depth profiling of thin films, enabling accurate analysis of film density, porosity, and ion distribution under different electrochemical conditions.

OECT Device Fabrication and Characterization: Polymer solutions of P3HT were prepared at a concentration of 5 mg mL^{-1} in chlorobenzene and chloroform and denoted as CB and CF, respectively. Fiber solutions were prepared by adding 10 vol% ACN to the P3HT CB solution containing 20 mol% salt additives. The solutions were then ultrasonicated for 10 minutes, followed by UV irradiation at 365 nm for 10 minutes. The resulting samples were labeled as pristine, KPF_6, $TBAPF_6$, and 18-O-6, corresponding to the specific salt additives. Film thickness was consistently maintained between 30 and 40 nm. Devices were fabricated following a conventional top-gate/bottom-contact (TG/BC) structure: glass substrates cleaned with acetone and isopropanol were sequentially coated with chromium (5 nm) and gold (40 nm) at a deposition rate of 0.5 Å s^{-1} under high vacuum conditions (< 5×10^{-6} torr). The interdigitated electrodes featured a channel length of 80 μm and a width of 1000 μm. P3HT solutions were spin-coated onto plasma-treated electrode surfaces at 1,000 rpm for 60 seconds, and film thickness was measured using an Alpha-Step D300 profilometer.

Device measurements were performed using a Keithley 4200-SCS parameter analyzer under vacuum. Transfer characteristics were recorded by sweeping gate voltages (V_g) from 0 to −0.7 V with a scan rate of 10 mV/s at a fixed drain voltage (V_d) of −0.5 V. Transconductance (g_m) was calculated using Equation **(1)**:

$$g_m = \frac{\partial I_d}{\partial V_g} = \frac{W d_{norm}}{L} \mu C^* (V_{th} - V_g) \quad (1)$$

where $d_{norm} = d \times \varepsilon$, d is the measured film thickness, and ε is the surface coverage index, reflecting the normalized film thickness for nanofiber films considering their porous structure. Normalized transconductance ($g_{m,norm}$) was calculated to ensure consistent comparison across devices using the equation $g_{m,norm} = g_m/(Wd/L)$. The threshold voltage (V_{th}) was extracted from linear fits to the $I_d^{1/2}$

versus V_g curves. Carrier density (p) was calculated from integrated gate current transfer curves based on Equation **(3)**. The carrier density shown in **Figs. S8** and **S13** were extracted by integrating the electrochemical charge under the assumption that the injected ionic charge corresponds to reversible volumetric doping within the active polymer volume. This approach assumes (i) a one-to-one correspondence between injected ionic charge and electronic carriers, (ii) negligible contribution from irreversible side reactions within the selected voltage window, and (iii) uniform participation of the electrochemically active volume. The integration was intentionally limited to –0.6 V, which is the $g_{m,norm}$ maximal position, to reflect the practical operating conditions used in device measurements and temporal current retention tests. In the OECT operations of this study, the gate voltage does not exceed this value to maintain device stability and avoid parasitic faradaic processes. Integrating V_g beyond –0.6 V would potentially include additional electrochemical processes that are not relevant to steady-state transistor operation and may artificially inflate the calculated carrier density.

Accurate mobility (μ) was extracted from Equation **(2)**, in which μ and p are mobility and concentration of the charge carriers, respectively. The coefficient α is defined by experimental parameters, specifically device geometry parameters (channel width W, channel length L, and channel thickness d), elementary charge (e), and the drain voltage (V_d), following the relation $\alpha = (WdeV_d)/(L)$. The determination of μC^* was calculated by multiplying μ from equation **(2)** and C^* from the EIS Bode plot.

$$I_d = \mu p \alpha \tag{2}$$

$$p = \frac{\int I_g dV_g}{r_v eAd} \tag{3}$$

Mobility in OECTs is not a directly measurable quantity but a model-dependent parameter that relies on assumptions regarding carrier density, volumetric capacitance, and device operation regime. As discussed by Mariani et al. (*Small*, 2019, **15**, 1902534), the mobility in working OECTs is commonly treated as an effective mobility, which incorporates contributions from carrier density variations,

contact resistance, and device geometry. The extraction of μ is therefore intrinsically dependent on the adopted physical model and experimental configuration. In this study, μ derived from steady-state temporal I_d represents an effective mobility consistent with the steady-state μC^* framework. Therefore, the μ extraction is model-dependent but yields physically reasonable values that are internally consistent with the steady-state volumetric capacitance and transconductance analysis.

Output curves were recorded by adjusting V_g from 0 to −0.8 V in increments of 0.2 V, with a 0.5-second interval between steps. A dual sweep was applied to return the device to its initial state. Transient curves were measured using pulsed V_g (0 and −0.7 V), each pulse lasting 15 seconds, with the drain voltage fixed at −0.5 V. Rise time (t_r) and fall time (t_f) were calculated by fitting the transient curves with an exponential function $y = y_0 + A_1 \exp(-x/t_1)$, where y is I_d, x is the time, and t_1 represents t_r or t_f. Device stability was evaluated by repeatedly applying pulsed gate voltages of 0 and −0.7 V, each lasting 15 seconds, at a fixed drain voltage of −0.5 V, for 60 consecutive cycles.

Electrochemical impedance spectroscopy (EIS) and cyclic voltammetry (CV) analyses were performed using the same electrochemical cell arrangement as described previously. Multiple electrode geometries with surface areas ranging from 0.5 to 4.0 cm^2 were fabricated on glass substrates. EIS measurements were conducted in a conventional three-electrode configuration, with the working electrode (WE) consisting of polymer-coated gold electrodes and the counter electrode (CE) a platinum wire. The reference electrode (RE) was an Ag/AgCl electrode. All electrodes were immersed in a 0.1 M KPF_6 aqueous solution. The potential of the working electrode was varied in increments of –0.1 V, with an AC perturbation of 10 mV superimposed. The capacitance (C) was extracted from the imaginary component of the impedance using equation **(4)**.

$$C = \frac{1}{2\pi f |Z''|} \tag{4}$$

To determine the volumetric capacitance (C^*), the measured capacitance was normalized by the volume of the electrode. For device characterization, a 0.1 M aqueous KPF_6 electrolyte solution was

retained within a polydimethylsiloxane (PDMS) well. An Ag/AgCl pseudo-reference pellet served as the gate electrode.

Table S1. Surface coverage ratio calculated from the algorithm based on the AFM morphology.

	Pristine	**KPF_6**	**$TBAPF_6$**	**18-O-6**
As-cast	54.21 %	40.24 %	57.77 %	50.96 %
Doped	51.32 %	44.45 %	56.77 %	60.67 %
Dedoped	51.46 %	39.59 %	57.83 %	51.05 %

Table S2. Comparison between the coverage index (ε) derived from the algorithm based on AFM morphology and NR methods.

	Pristine	**KPF_6**	**$TBAPF_6$**	**18-O-6**
AFM algorithm	0.826	0.614	0.881	0.777
NR	$\leq$ 0.938±0.040	$\leq$ 0.710±0.257	$\leq$ 0.763±0.051	$\leq$ 0.885±0.054

Table S3. SLD values evaluated by NR analysis of the films in different states.

	Pristine	**KPF6**	**TBAPF6**	**18-O-6**
As cast	0.576±0.025	0.607±0.022	0.436±0.029	0.559±0.034
Doped	0.780±0.024	0.783±0.020	0.648±0.037	0.841±0.043
Dedoped	0.642±0.033	0.662±0.026	0.497±0.025	0.464±0.023

Table S4. Estimated volume fraction of the PF_6^- anion contained within the OECT channel thin films at the doped or dedoped states. The calculation is based on the SLD variations in the NR analysis.

	Pristine	**KPF_6**	**$TBAPF_6$**	**18-O-6**
Doped	0.242	0.209	0.217	0.361
Dedoped	0.067	0.057	0.054	--

Table S5. Summary of the *d*-spacing (*d*), coherence length (L_c), and paracrystalline disorder (*g*) of lamellar stacking of the pristine, KPF_6, $TBAPF_6$, and 18-O-6 films.

		q (Å^{-1})	FWHM (Å^{-1})	d (Å)	L_c (Å)	g
Pristine	As-cast	0.45	0.059	13.8	96.0	0.143
	Doped	0.44	0.055	14.4	102.7	0.142
	Dedoped	0.46	0.055	13.8	102.9	0.139
KPF_6	As-cast	0.46	0.049	13.6	116.4	0.130
	Doped	0.44	0.061	14.1	92.8	0.148
	Dedoped	0.44	0.052	14.3	109.5	0.137
$TBAPF_6$	As-cast	0.46	0.055	13.7	102.4	0.139
	Doped	0.45	0.062	14.0	91.9	0.148
	Dedoped	0.46	0.058	13.7	97.6	0.142
18-O-6	As-cast	0.47	0.055	13.4	102.4	0.137
	Doped	0.46	0.056	13.7	101.0	0.139
	Dedoped	0.46	0.059	13.7	95.7	0.143

Table S6. GIXD crystallographic parameters of the pristine, KPF_6, $TBAPF_6$, and 18-O-6 films derived from the geometrically corrected azimuthal integral profiles.

Parameters	OOP/(IP+OOP)			rDOC (%)		
States	As-cast	Doped	Dedoped	As-cast	Doped	Dedoped
Prisitne	0.874	0.800	0.780	100%	91%	89%
KPF6	0.712	0.753	0.799	81%	86%	91%
TBAPF6	0.671	0.609	0.740	77%	70%	85%
18-O-6	0.730	0.834	0.716	83%	95%	82%

Table S7. Literature summary of the performance of p-type OMIECs in OECTs.

Polymer	$\boldsymbol{\mu C^*}$ **(F cm^{-1} V^{-1} s^{-1})**	**C* (F cm^{-3})**	$\boldsymbol{\mu}$ **(cm^2 V^{-1} s^{-1})**	$\mathbf{V_{th}}$ **(V)**	**Year**	**Ref**
P3HT+KPF_6	267 ± 13	98 ± 1	2.73 ± 0.13	–0.37 ± 0.02	2026	This work
PBTTT	960 ± 30	390 ± 40	2.5 ± 0.3	–0.32 ± 0.06	2025	S-1
PE_2-OE_4	830 ± 37	207 ± 19	4.0 ± 0.6	0.24 ± 0.06	2024	S-2
PDPP-4EG	804 ± 7	103 ± 3	7.83 ± 0.05	--	2024	S-3
P(3g2T-T)+CB+BCF	556	166	3.35 ± 0.26	–0.06	2022	S-4
P(g2T-TT)	299 ± 5	171 ± 8	1.82 ± 0.09	0.00 ± 0.01	2019	S-5
P(bgDPP-MeOT2)	195	120	1.63	–0.33	2022	S-6

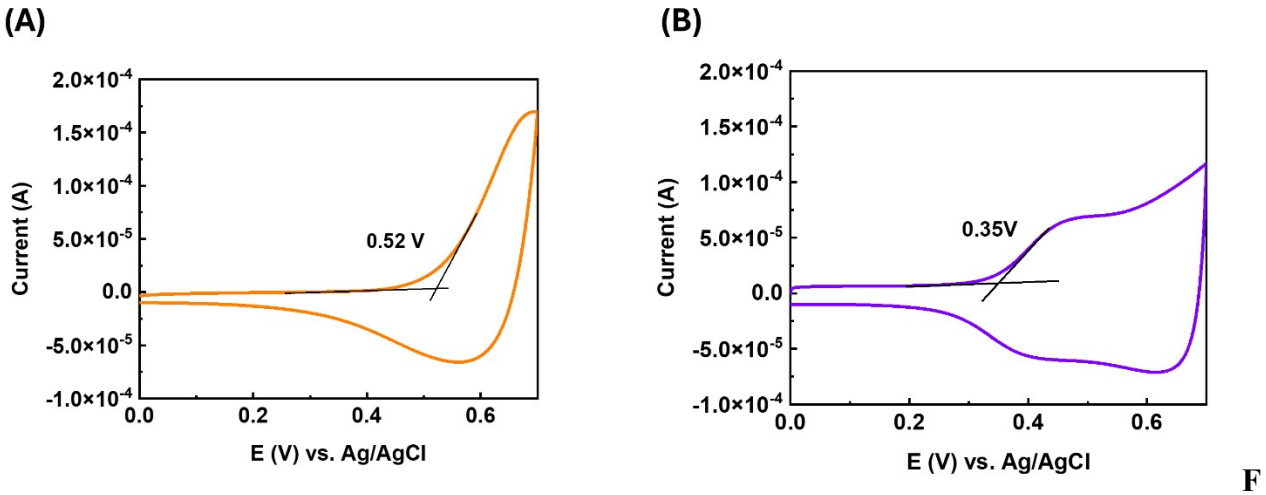

Fig. S1. CV profiles of the polymer films coated with (a) CB and (b) CF in 0.1 M KPF_6, with fitted onset voltages.

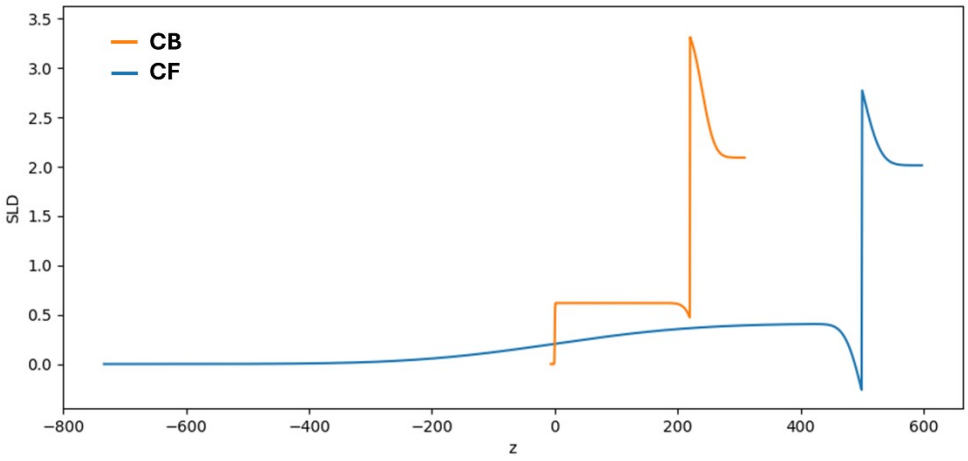

Fig. S2. NR SLD profile of the dense (CB) and porous (CF) P3HT films coated from a chlorobenzene or chloroform solution.

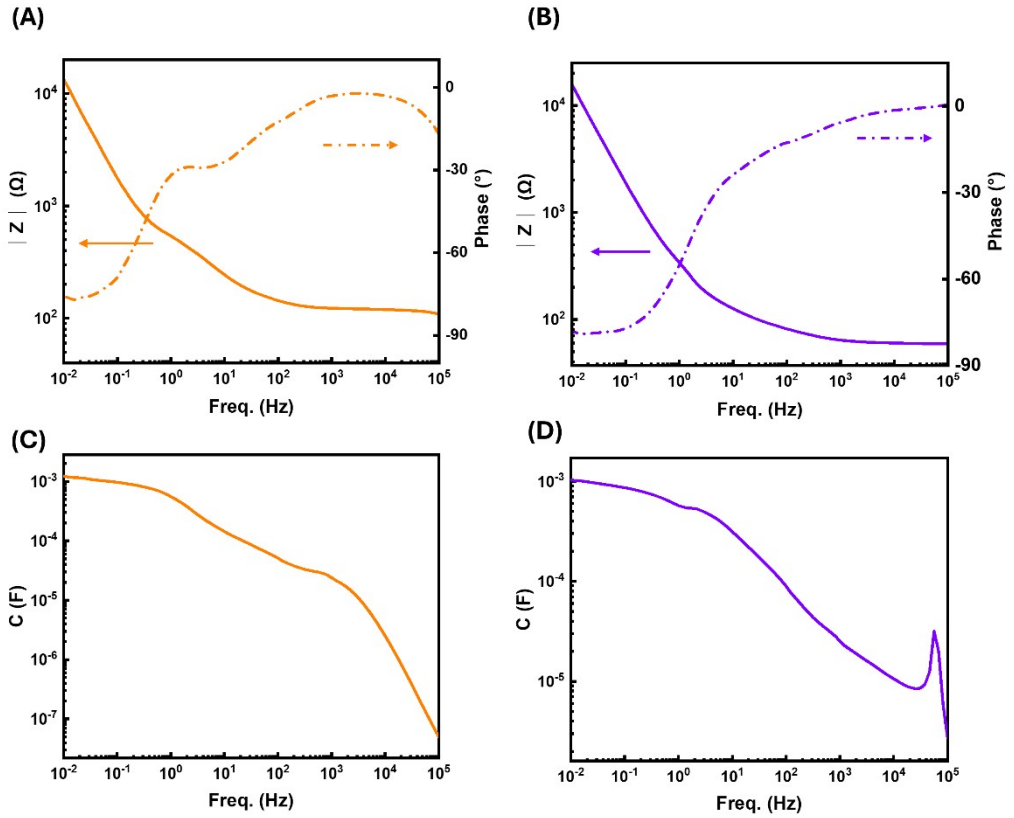

Fig. S3. Bode plot of the (a) dense CB film coated with chlorobenzene and (b) porous CF film coated with chloroform (|Z| vs. frequency, and phase vs. frequency). Effective capacitance spectrum of the electrochemically doped (c) CB and (d) CF film. The data were recorded at an offset bias (V_{offset}) of –0.6 V vs. Ag/AgCl reference electrode.

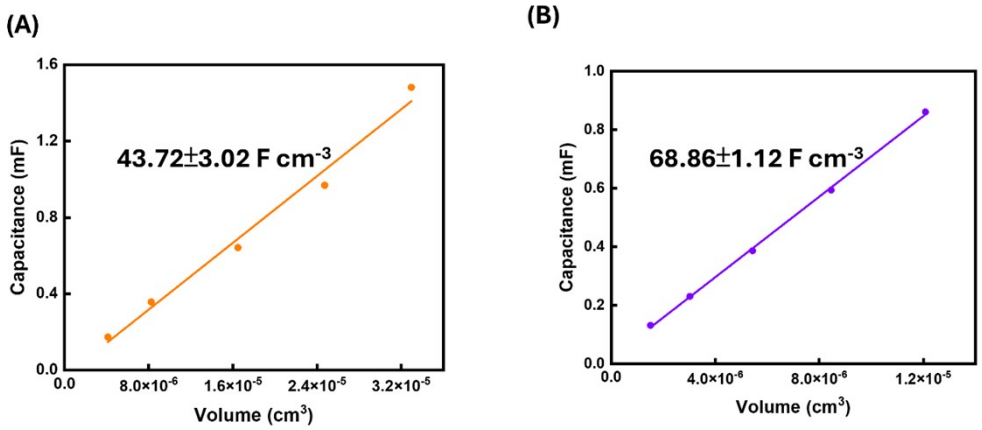

Fig. S4. The effective volumetric capacitance of (a) CB and (b) CF films at f = 0.1 Hz for the linear fitting of C^*.

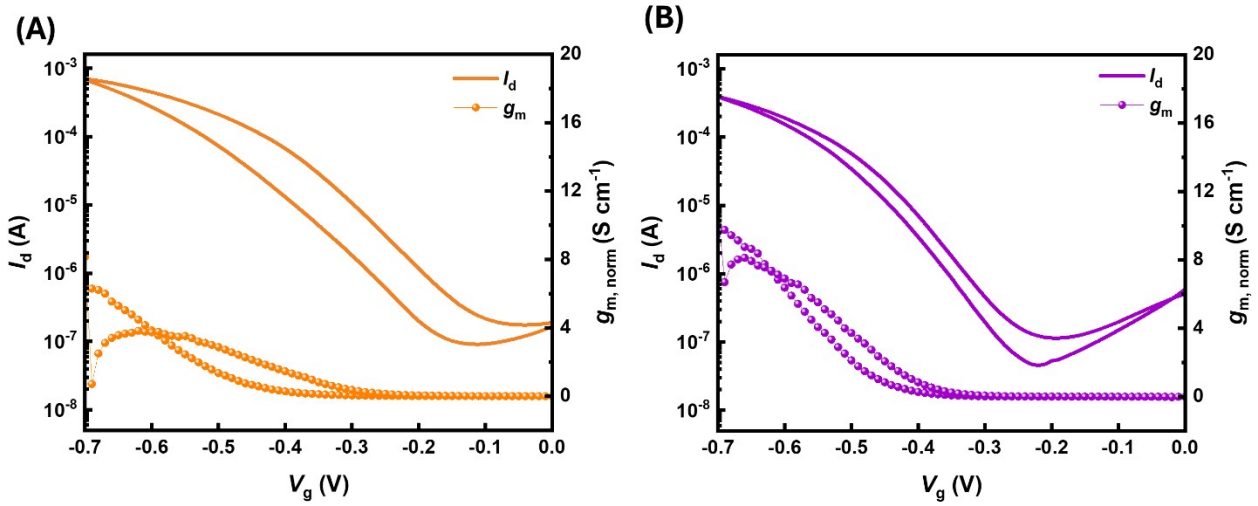

Fig. S5. Transfer curves of the (a) CB and (b) CF polymer film OECTs operated in 0.1 M KPF_6. The measurements were conducted at V_d = –0.6 V and the V_g was forward swept from 0 to –0.7 V at a scan rate of 10 mV s^{-1}.

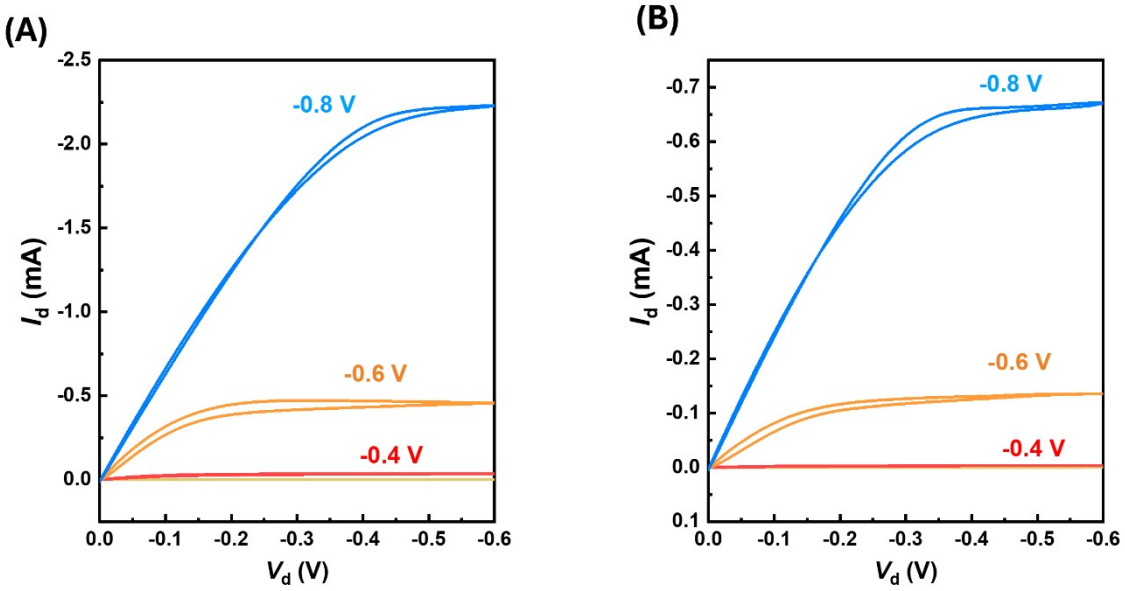

Fig. S6. Output curves of the OECT devices based on (a) CB and (b) CF with 0.1 M $KPF_{6(aq)}$ as an electrolyte at different V_g spanning the range of 0 to –0.8 V. Note that the V_d was linearly swept from 0 to –0.6 V at a scan rate of 10 mV s^{-1}.

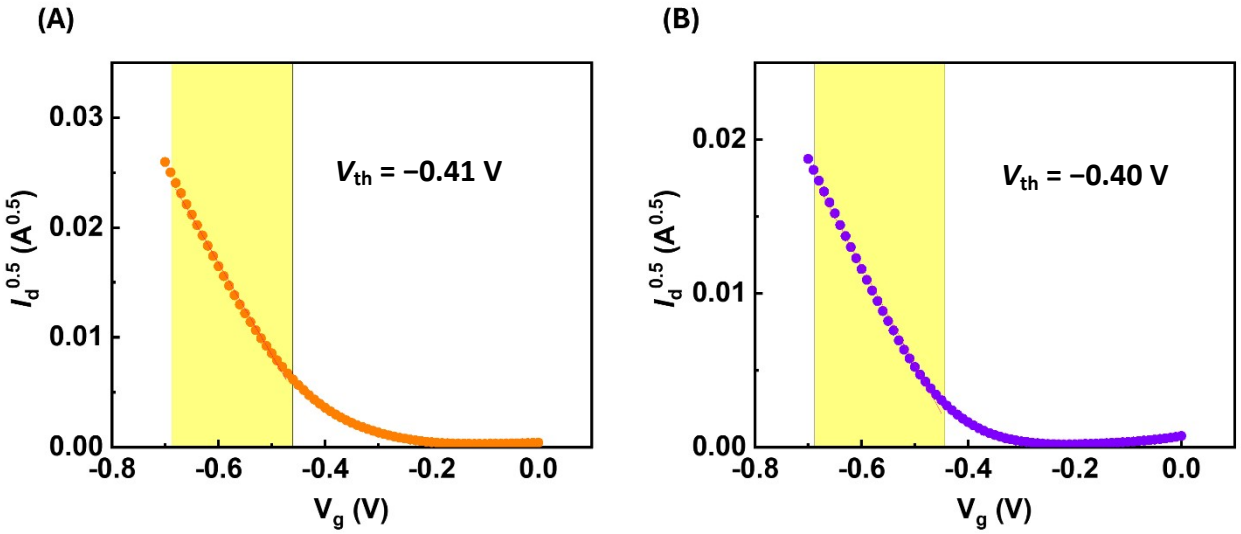

Fig. S7. Threshold voltage fittings of the OECT devices based on the transfer characteristics of (a) CB and (b) CF with 0.1 M $KPF_{6(aq)}$ as an electrolyte. Note that the V_g was linearly swept from 0 to –0.7 V.

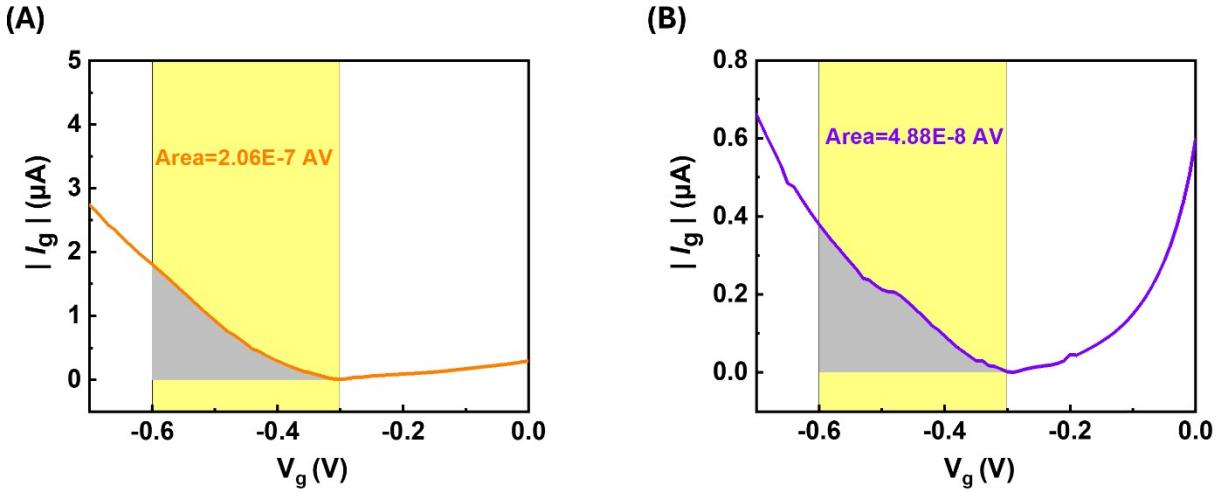

Fig. S8. Determination of the p values by integrating the area of I_g vs. V_g plots derived from the transfer characteristics for the (a) CB and (b) CF based OECTs. Note that the V_g was linearly swept from 0 to –0.7 V.

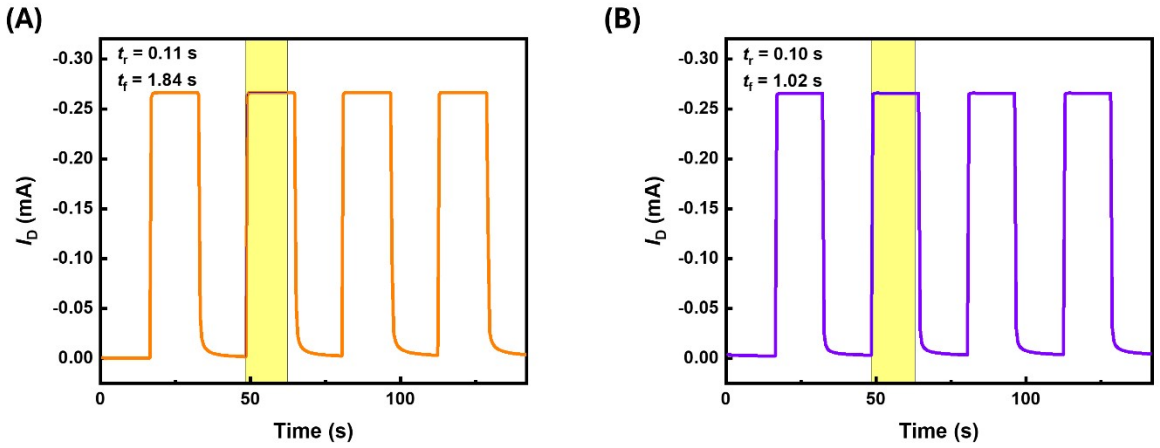

Fig. S9. Transient characteristics of the OECT devices comprising (a) CB and (b) CF with 0.1 M $KPF_{6(aq)}$ as an electrolyte. Note that the V_g was switched between 0 and –0.7 V every 15 s, and V_d was fixed at −0.5 V.

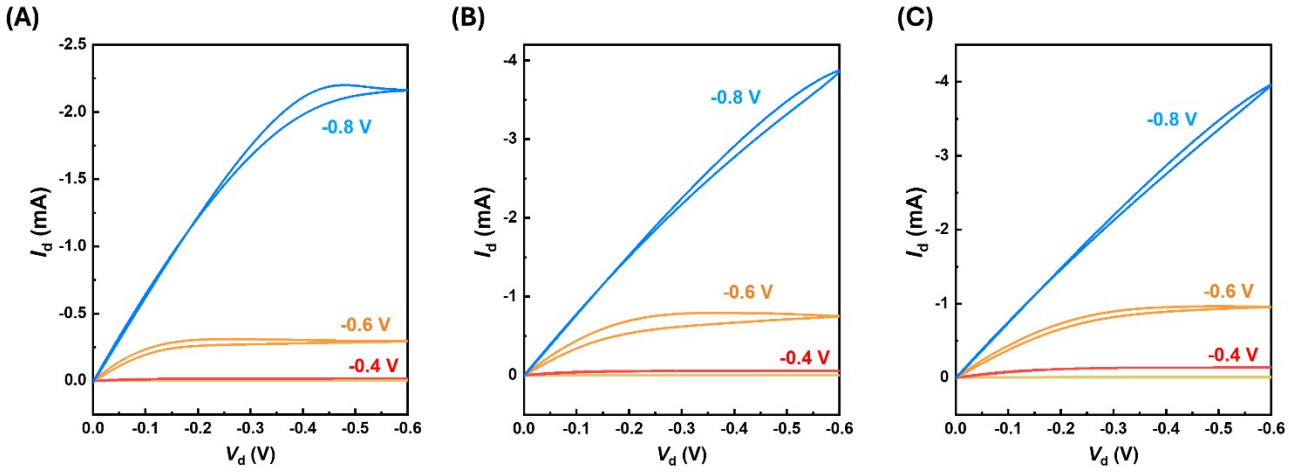

Fig. S10. Output characteristics of the OECT devices based on (a) pristine, (b) $TBAPF_6$ and (c) 18-O-6 films with 0.1 M $KPF_{6(aq)}$ as an electrolyte at different V_g spanning the range of 0 to –0.8 V. Note that the V_d was linearly swept from 0 to –0.6 V at a scan rate of 10 mV s^{-1}.

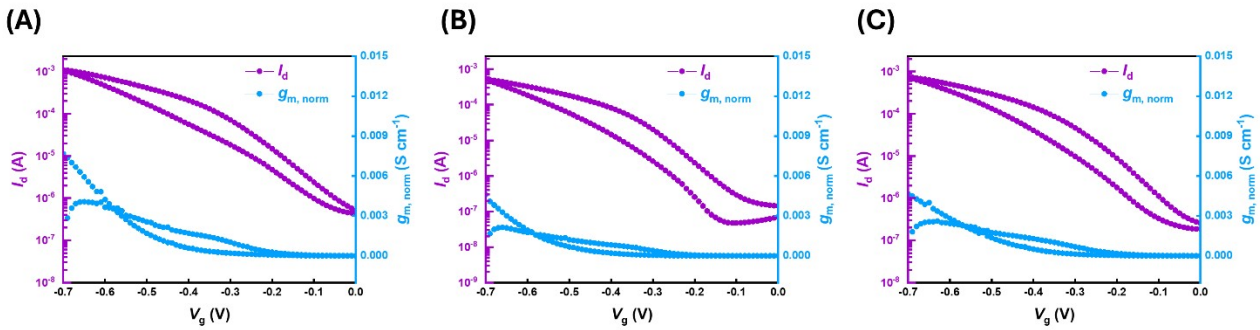

Fig. S11. Transfer curves of the OECT devices based on (a) pristine, (b) $TBAPF_6$ and (c) 18-O-6 films with 0.1 M $KPF_{6(aq)}$ as an electrolyte at a fixed V_d of –0.5 V. Note that the V_g was forward swept from 0 to –0.7 V at a scan rate of 10 mV s^{-1}.

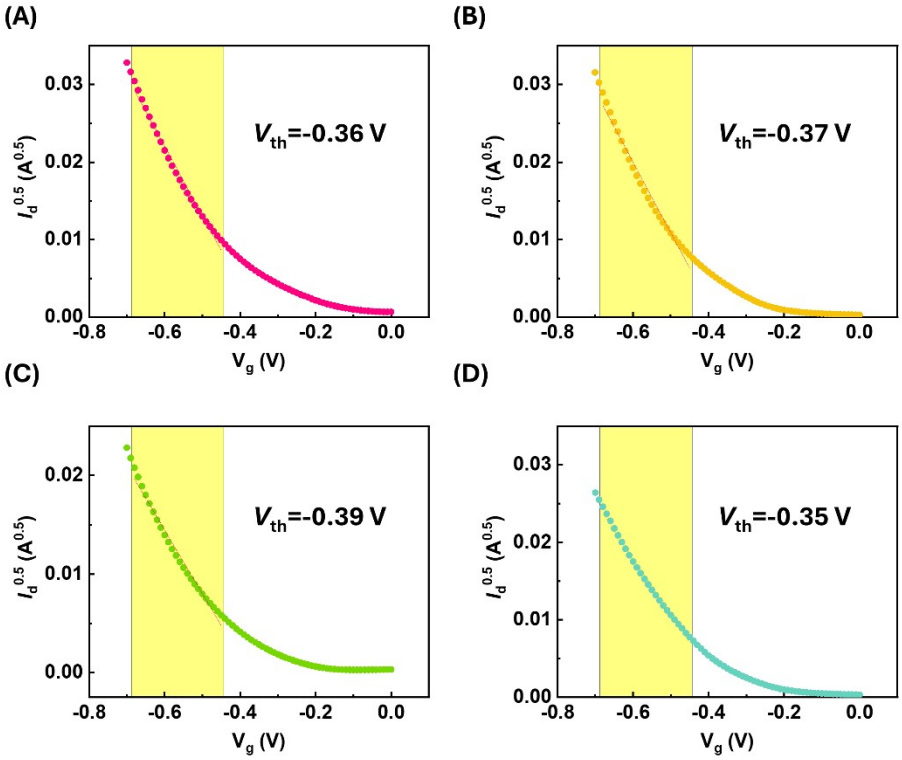

Fig. S12. Threshold voltage fittings of the (a) pristine and films with salt additives: (b) KPF_6, (c) $TBAPF_6$, and (d) 18-O-6 OECT devices with 0.1 M $KPF_{6(aq)}$ as an electrolyte. Note that the V_g was linearly swept from 0 to –0.7 V.

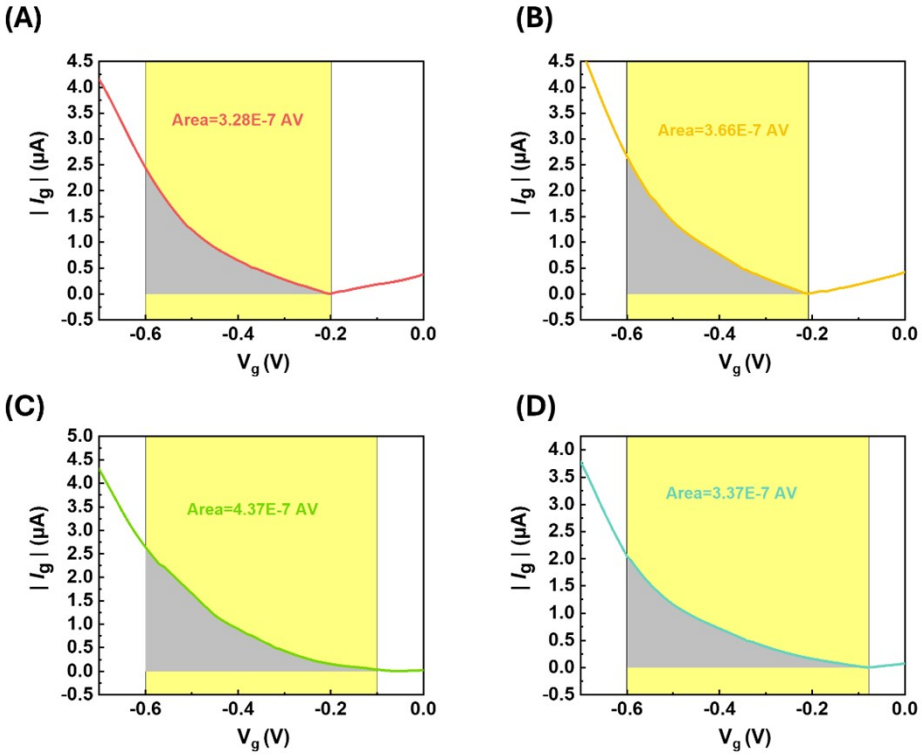

Fig. S13. Determination of the p values by integrating the area of I_g vs. V_g plots for the (a) pristine and films with salt additives: (b) KPF_6, (c) $TBAPF_6$, and (d) 18-O-6 OECT devices with 0.1 M $KPF_{6(aq)}$ as an electrolyte. Note that the V_g was linearly swept from 0 to –0.7 V.

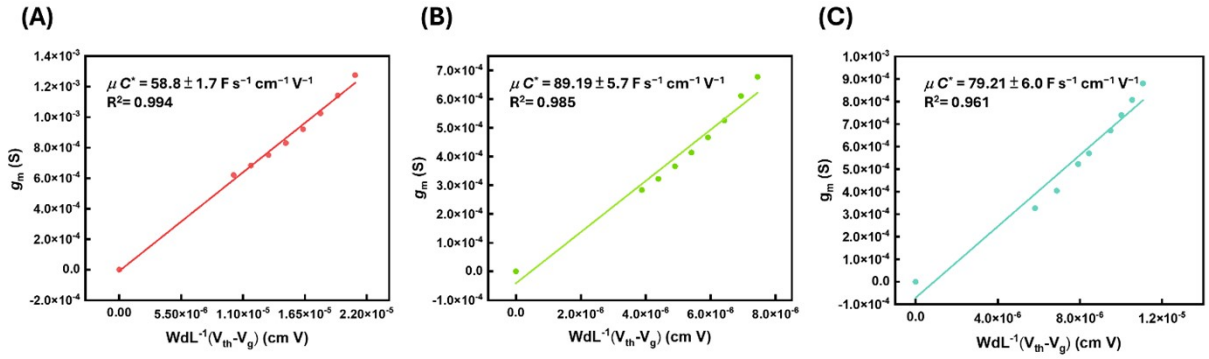

Fig. S14. Determination of the μC^* values by linear fitting of g_m vs. $WdL^{-1}(V_{th} - V_g)$ for (a) Pristine, (b) $TBAPF_6$, and (d) 18-O-6 based OECTs, and the corresponding coefficients of determination (R^2) are indicated in each panel.

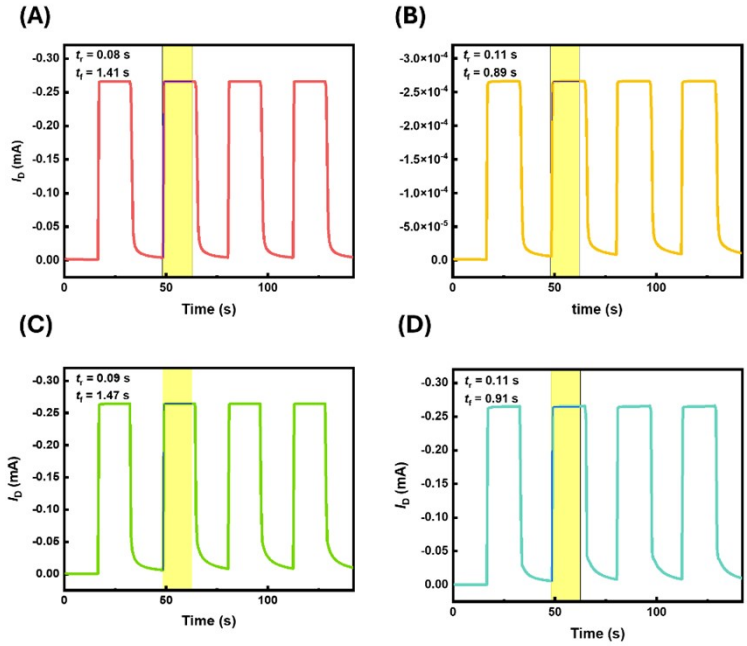

Fig. S15. Transient characteristics of the OECT devices based on: (a) pristine, (b) KPF_6, (c)$TBAPF_6$, and (d) 18-O-6 with 0.1 M $KPF_{6(aq)}$ as an electrolyte. Note that the V_g was switched between 0 and –0.7 V every 15 s, and V_d was fixed at −0.5 V.

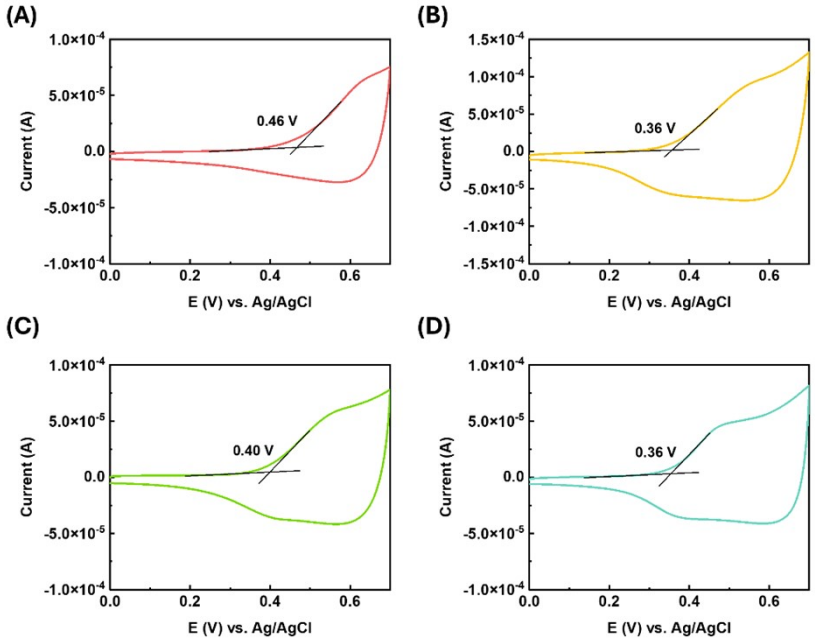

Fig. S16. CV profiles of the conjugated nanofiber films in an electrolyte of 0.1 M $KPF_{6(aq)}$: (a) pristine, (b) KPF_6, (c) $TBAPF_6$, and (d) 18-O-6. Note that the scan rate of CV is 0.1 V s^{-1}.

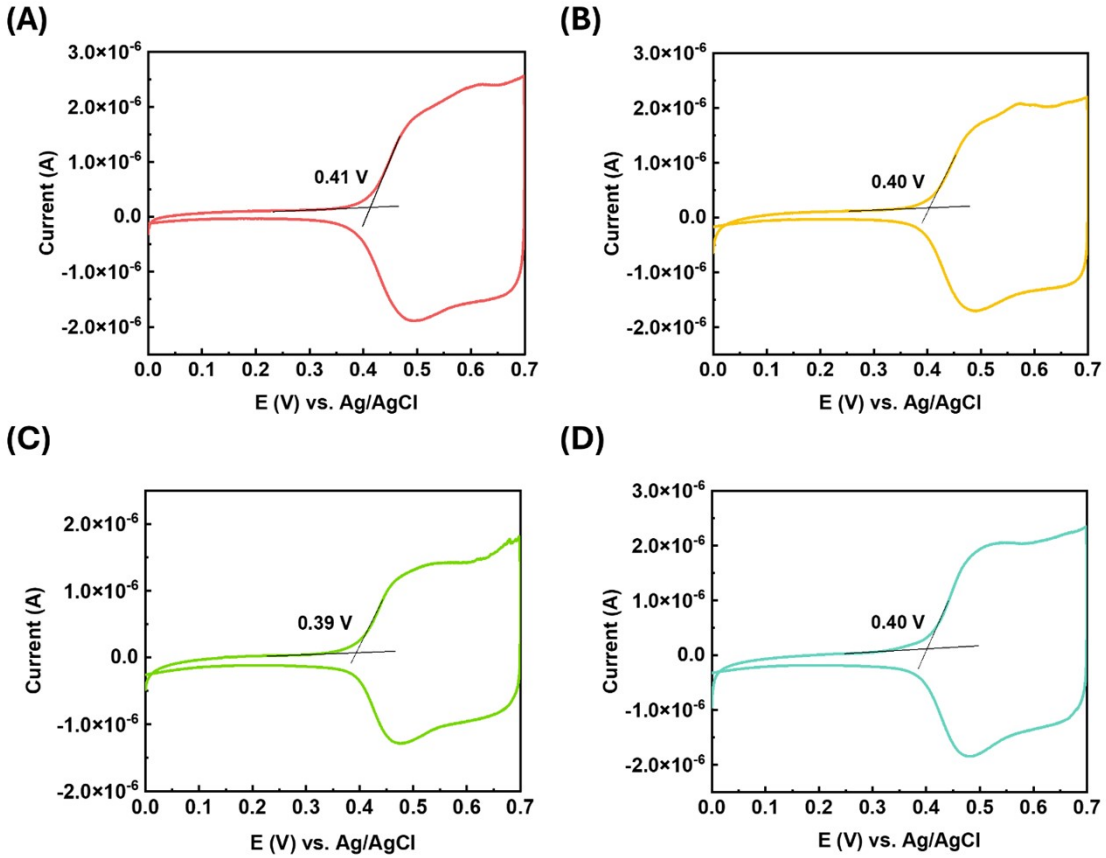

Fig. S17. CV profiles of the conjugated nanofiber films in an electrolyte of 0.1 M $KPF_{6(aq)}$: (a) pristine, (b) KPF_6, (c) $TBAPF_6$, and (d) 18-O-6. Note that the scan rate of CV is 0.1 mV s^{-1}.

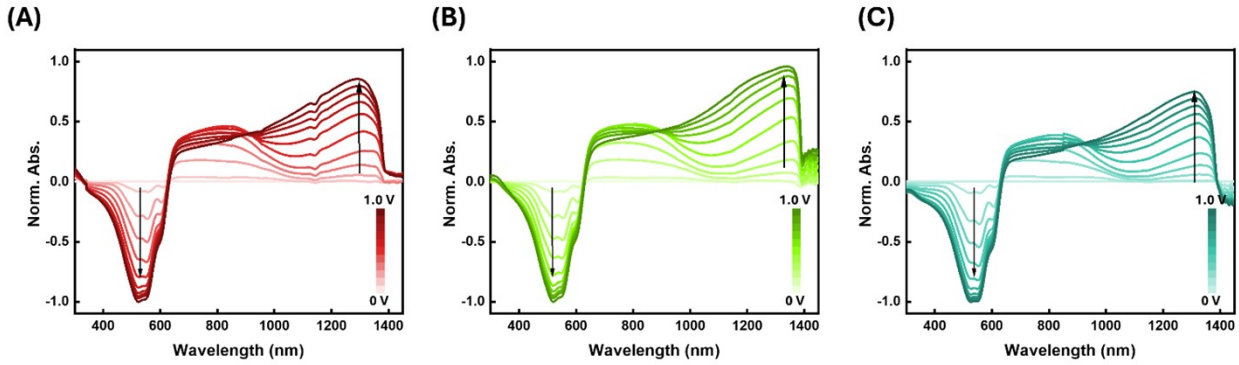

Fig. S18. In-situ electrochemical–optical spectra of the conjugated nanofiber films of (a) pristine, (b) $TBAPF_6$, and (c) 18-O-6. Note that the working electrode is an ITO glass coated with the thin films, the counter electrode is the Pt rod, the reference is the Ag/AgCl electrode, and the electrolyte is 0.1 M $KPF_{6(aq)}$. The voltage was step-wise increased from 0 to 1.0 V with a step of 0.1 V.

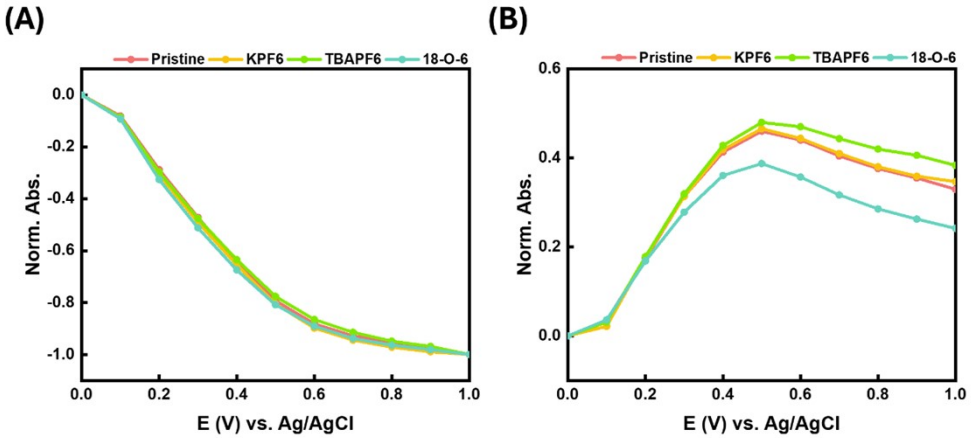

Fig. S19. The optical absorbance changes in the characteristic peaks of (a) Neutral specie band at 530 nm and (b) intermediate peak at 809 nm derived from the in-situ electrochemical–optical spectra of the conjugated nanofiber films.

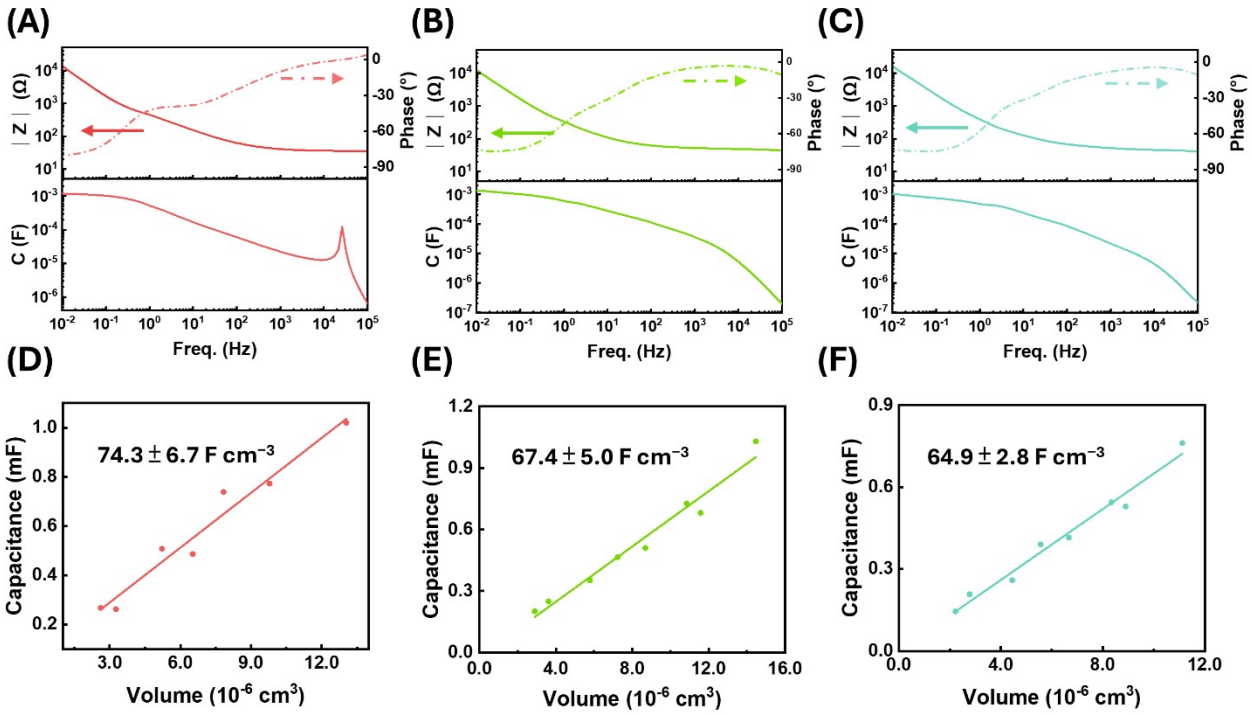

Fig. S20. Bode plot (|Z| vs. frequency, and phase vs. frequency) and effective capacitance spectrum of an electrochemically doped (a) pristine, (b) TBAPF6, and (c) 18-O-6 films. The data were recorded at an offset bias (V_{offset}) of -0.7 V vs. Ag/AgCl. The effective volumetric capacitance of the (d) pristine, (e) TBAPF6, and (f) 18-O-6 films under different geometries. Values were reported at f = 0.1 Hz, and C^* was calculated from the linear fit.

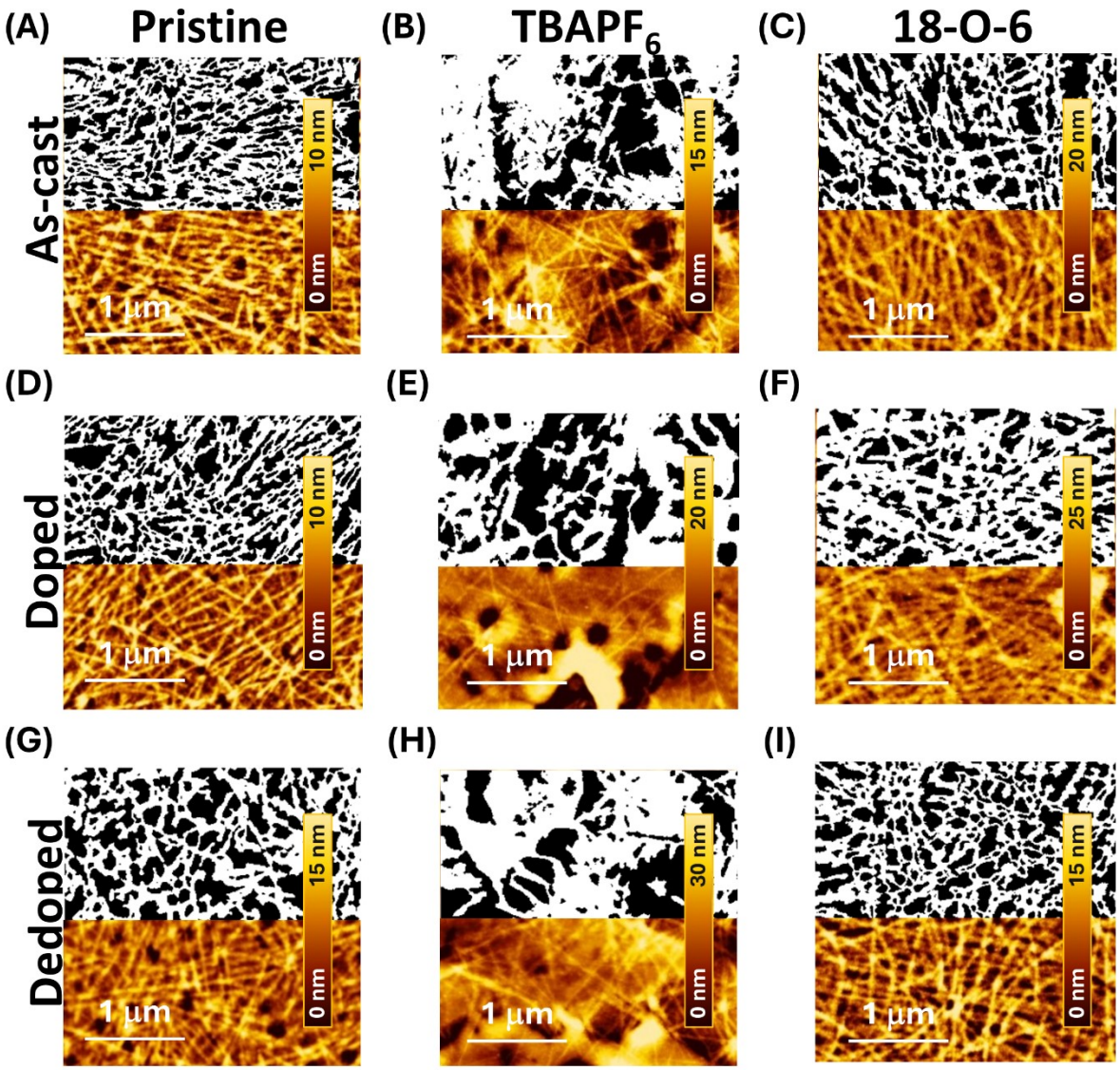

Fig. S21. AFM height images and algorithm analysis of the (a–c) as-cast films, (d–f) ex-situ doped films, and (g–i) ex-situ dedoped films of (a,d,g) Pristine, (b,e,h) TBAPF6, and (c,f,i) 18-O-6. The size of the images are 3 μm × 3 μm. Note that the doping was conducted at 0.7 V, and the dedoping was conducted by linearly sweeping the potential from 0.7 to 0 V.

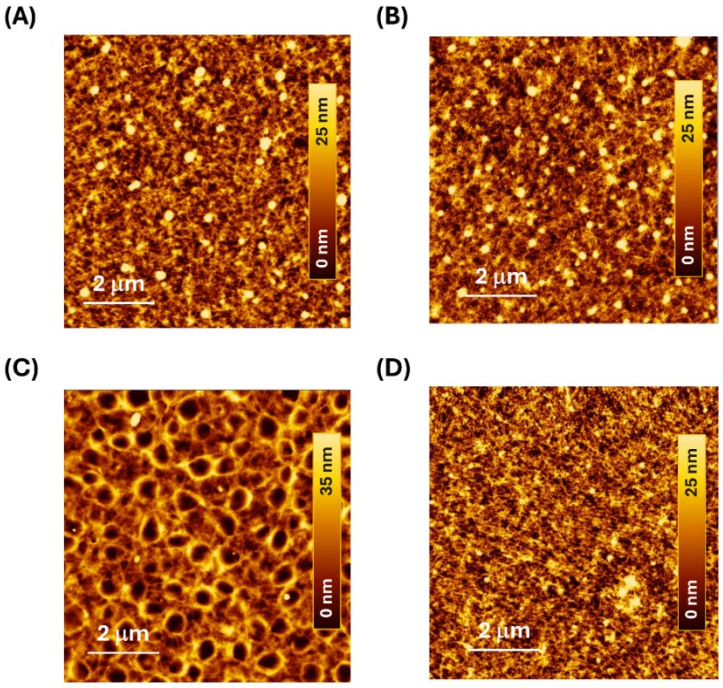

Fig. S22. AFM height images with larger scan scale of the (a) Pristine, (b) KPF_6, (c) $TBAPF_6$, and (d) 18-O-6. The size of the images are 8 μm × 8 μm.

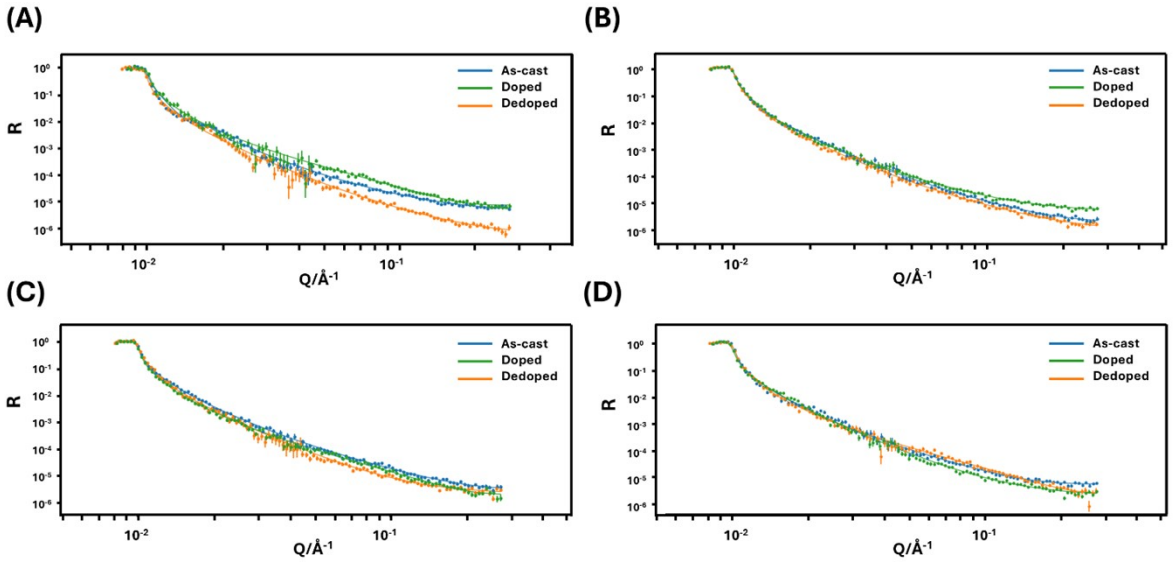

Fig. S23. NR reflectivity of *R* vs change in momentum transfer of *Q* of the conjugated nanofiber films of (a) pristine, (b) KPF_6, (c) $TBAPF_6$ and (d) 18-O-6. The inset contains the SLD profile obtained from the fit. Note that the doping was conducted at –0.7 V, and the dedoping was conducted by linearly sweeping the potential from –0.7 to 0 V.

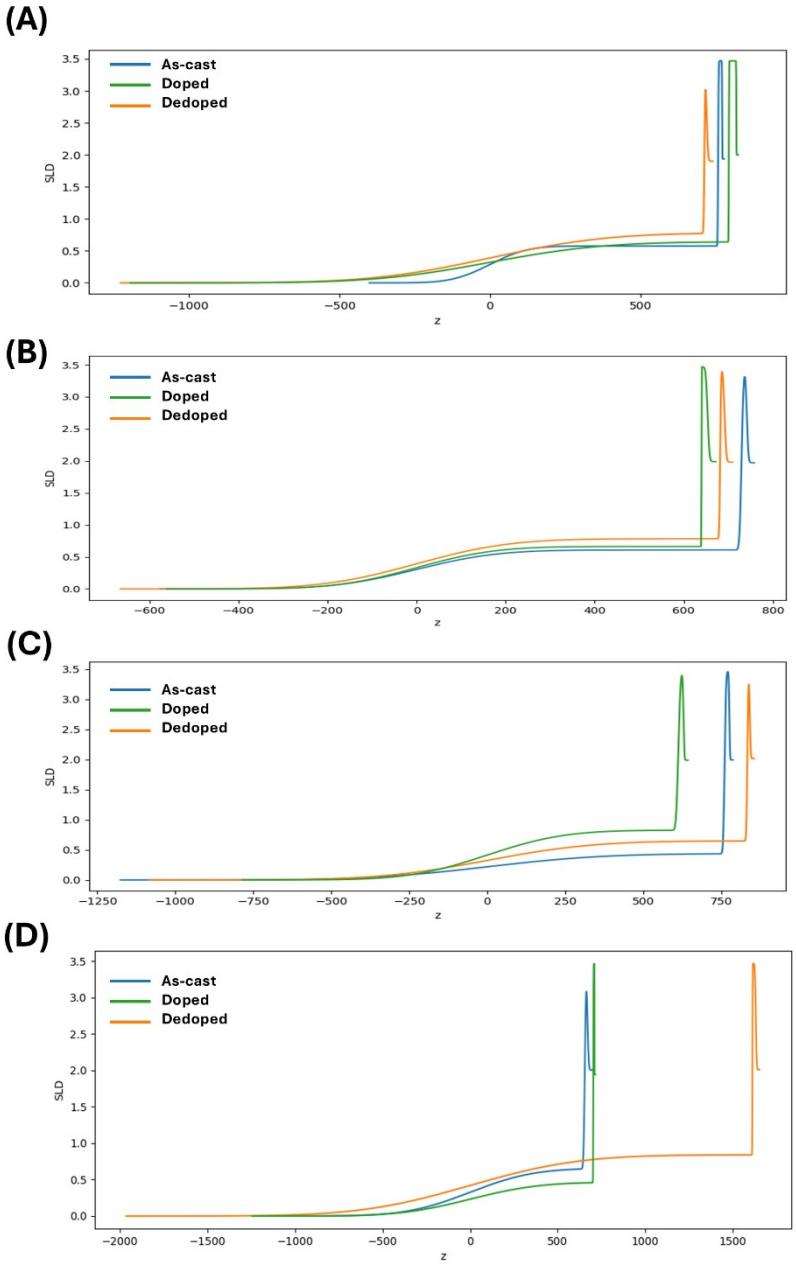

Fig. S24. NR SLD profiles of the conjugated nanofiber films: (a) pristine, (b) KPF_6, (c)$TBAPF_6$, and (d) 18-O-6.

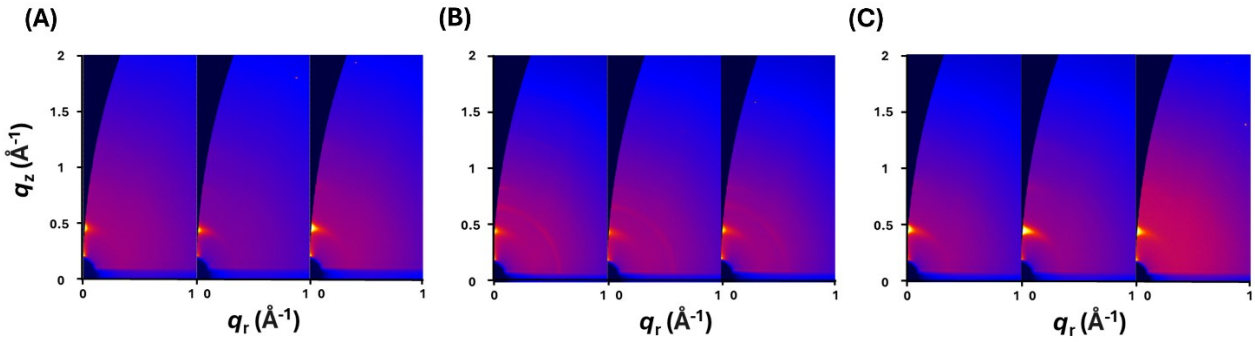

Fig. S25. 2D GIXD patterns of the (a) pristine and (b) $TBAPF_6$ and (c) 18-O-6 films, under conditions of as-cast (left), doped (middle), and dedoped (right). Doping was performed at 0.7 V, and dedoping was performed by linearly sweeping the potential from 0.7 to 0 V.

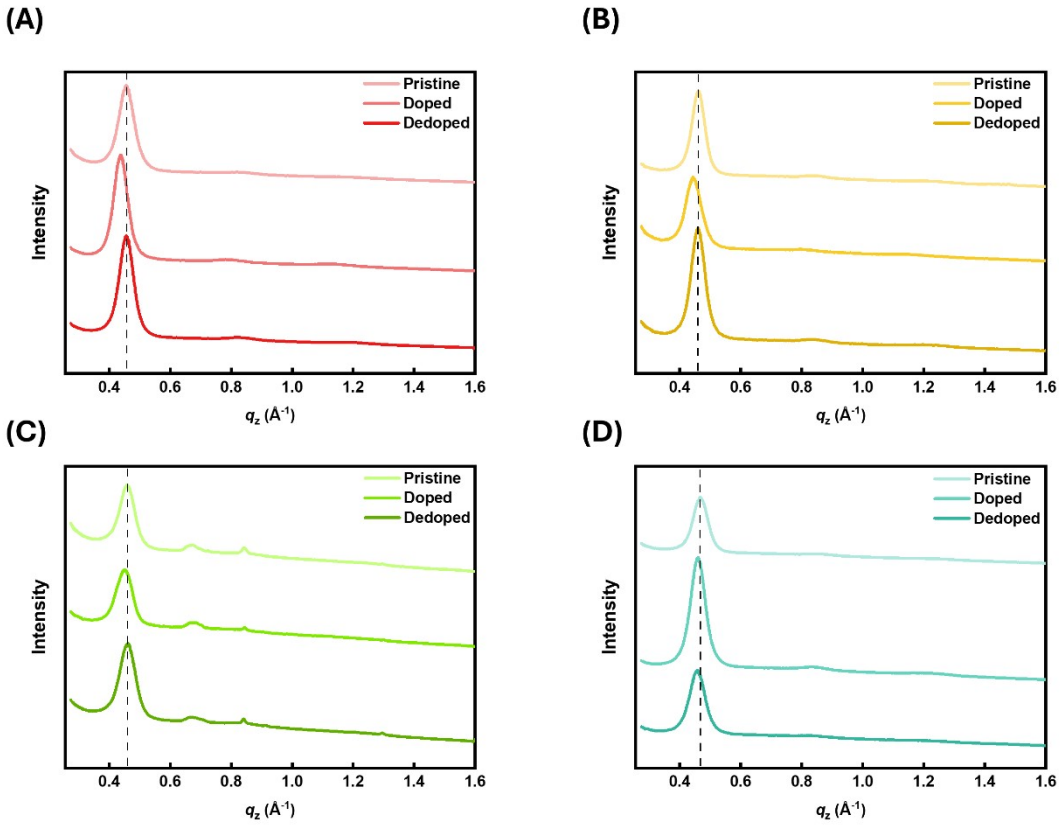

Fig. S26. 1D GIWAXS profile along the out-of-plane directions of the conjugated nanofiber films of (a) pristine, (b) KPF6, (c) TBAPF6, and (d) 18-O-6 films. The decreased/increased peak position indicates anion injection/ejection during the doping/dedoping processes.

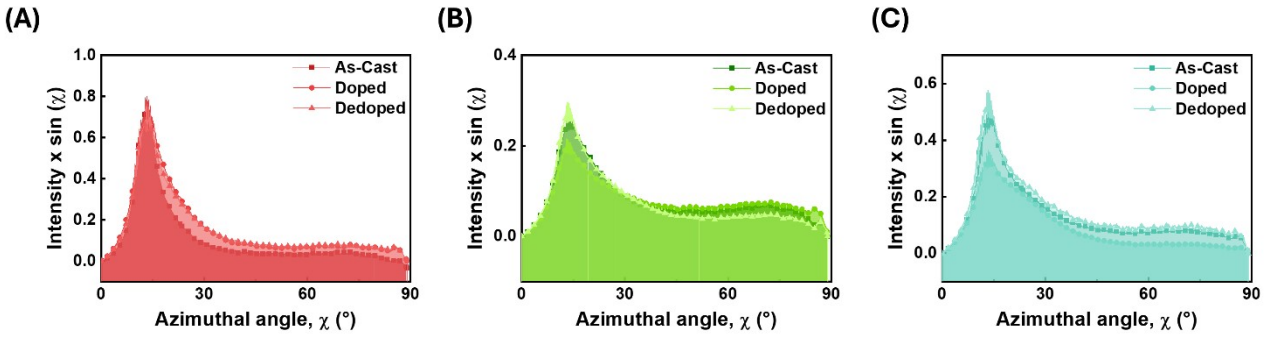

Fig. S27. Geometrically corrected pole figures of the (a) pristine, (b) TBAPF6 and (d) 18-O-6 films derived from the azimuthal integral of their (100) diffractions in 2D GIXD patterns.

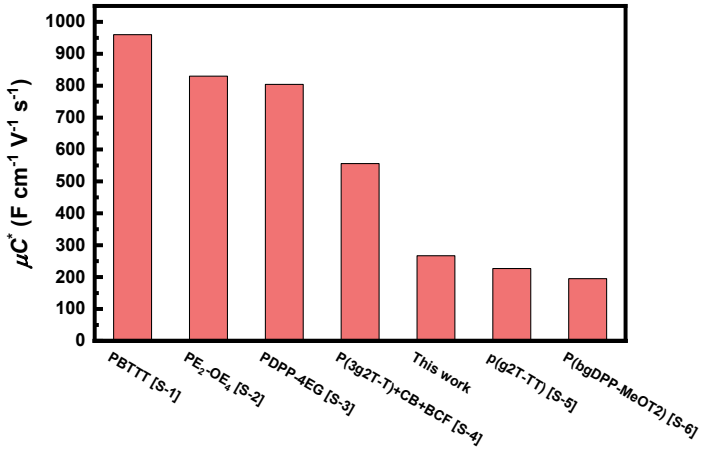

Fig. S28. Summary of the μC^* comparison of the recent p-type OECT studies.[S1-6]

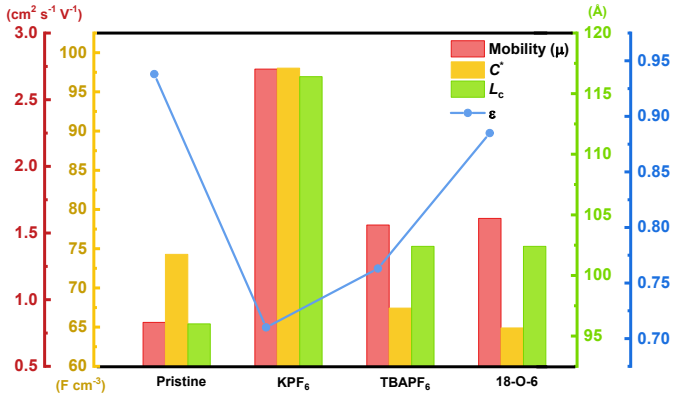

Fig. S29. Correlation between structural parameters of crystalline coherence length (L_c), NR-determined coverage ratio (ε), and device metrics, including the OECT mobility (μ) and volumetric capacitance (C^*) for thin films with different salt inclusions.

References in the Supporting Information

S-1 O. Bardagot, P. Durand, S. Guchait, H.-Y. Wu, I. Heinzen, W. Errafi, V. Bouylout, A. Pistillo, C.-Y. Yang, G. Rebetez, P. Cavassin, B. Jismy, J. Réhault, S. Fabiano, M. Brinkmann, N. Leclerc and N. Banerji, *Adv. Mater.*, 2025, **37**, 2420323.

S-2 O. Bardagot, B. T. DiTullio, A. L. Jones, J. Speregen, J. R. Reynolds and N. Banerji, *Adv. Funct. Mater.*, 2025, **35**, 2412554.

S-3 I.-Y. Jo, D. Jeong, Y. Moon, D. Lee, S. Lee, J.-G. Choi, D. Nam, J. H. Kim, J. Cho, S. Cho, D.-Y. Kim, H. Ahn, B. J. Kim and M.-H. Yoon, *Adv. Mater.*, 2024, **36**, 2307402.

S-4 T. C. Hidalgo Castillo, M. Moser, C. Cendra, P. D. Nayak, A. Salleo, I. McCulloch and S. Inal, *Chem. Mater.*, 2022, **34**, 6723-6733.

S-5 M. Moser, Y. Wang, T. C. Hidalgo, H. Liao, Y. Yu, J. Chen, J. Duan, F. Moruzzi, S. Griggs and A. Marks, *Mater. Horiz.*, 2022, **9**, 973-980.

S-6 P. Li and T. Lei, *J. Polym. Sci.*, 2022, **60**, 377-392.